

# Numerical simulations of asymmetric mixing in planar shear flows

By **F. F. GRINSTEIN,**

Berkeley Research Associates, PO Box 852, Springfield, VA 22152, USA

**E. S. ORAN AND J. P. BORIS**

Laboratory for Computational Physics, Naval Research Laboratory,  
Washington, DC, 20375, USA

(Received 13 November 1984 and in revised form 29 July 1985)

Numerical simulations were performed of the evolution of the Kelvin–Helmholtz instability in planar, free shear layers, resulting from coflow past a splitter plate. The calculations solved the time-dependent inviscid compressible conservation equations. New algorithms were developed and tested for inflow and outflow boundary conditions. Since no turbulence subgrid modelling was included, only the large-scale features of the flow are described. The transition from laminar flow was triggered by transverse pressure gradients and subsequent vorticity fluctuations at the shear layer, near the tip of the splitter plate. The calculations were performed for a range of free-stream velocity ratios and sizes of the chamber enclosing the system. The simulations showed that the resulting mixing layers have more of the faster fluid than the slower fluid entrained in the roll-ups. This effect is in general agreement with the results of recent splitter-plate experiments of Koochesfahani, Dimotakis & Broadwell (1983). The calculated mixing asymmetry is more apparent when the velocity ratio of the two streams is larger, and does not depend significantly on the separation between the walls of the chamber.

---

## 1. Introduction

This paper describes numerical simulations of shear flows and the development and evolution of coherent structures. There are two aspects of this problem which are addressed here. The first is developing the numerical model that was used in these studies. In particular, we are concerned with the treatment of inflow and outflow boundary conditions suitable for both compressible and incompressible flows. The second aspect is using this model to describe shear flows in a splitter-plate configuration.

The problem of developing the proper computational tools has been discussed previously (Boris *et al.* 1985). We elaborate on this subject in §3. The numerical model we use is a restructured version of the FAST2D computer code. This incorporates the Flux-Corrected Transport (FCT) continuity equation algorithm (Boris 1976*b*; Boris & Book 1976) which has been tested extensively for shock, blast, detonation, fluid instability and beam-generated turbulence calculations (e.g. Book *et al.* 1980; Oran *et al.* 1982; Picone & Boris 1983). Since the algorithm is explicit, the code is best for studying flows that move at a substantial fraction of the speed of sound in the material. Using timestep-splitting techniques, FCT may be coupled to algorithms representing other physical processes, such as diffusion and conduction (Oran & Boris 1981).

The second aspect, application of the model, is the main goal of this work. We have used the model to simulate time-dependent flows in the splitter-plate configuration for which substantial data exist on the transition to turbulence. Our interest here is in the entrainment and mixing in the resulting coherent structures in the flow. In §4 we describe the computational results and their implications.

## 2. Background

The development and structure of turbulent flows is the focus of intense study. We now know that flows which previously were thought to be totally chaotic and statistical in nature are dominated by the persistence of relatively large structures. These coherent structures were ignored since their existence was masked or de-emphasized by experimental averaging techniques. The classical description of turbulence and the mechanisms responsible for its development are now considered deficient in their explanations of these transient but organized and persistent structures which transport much of the stress in a shear layer.

The classical description of turbulence evolved from the observed behaviour of fluid flows as a function of Reynolds number. Many flows exhibit a series of sudden transitions to new flow patterns as the Reynolds number is increased. Each transition results in an increasingly complicated flow, and at high Reynolds number the flows become irregular and appear chaotic in both space and time. The transitions to the succession of flow patterns may be caused by a sequence of fluid instabilities, each of which breaks some symmetry in the previously stable flow pattern and introduces some new scale in the new flow pattern (Liepmann 1979). The transition to a purely chaotic flow was postulated to occur through an infinite succession of instabilities, each contributing to the increasing frequency content of the flow (Landau & Lifshitz 1959).

Several experimental observations have seriously eroded confidence in the completeness of such a turbulence model for physical flows. First, although laboratory-created grid turbulence comes close, no flow has yet been shown to exhibit pure, homogeneous isotropic turbulence in the classical sense. Such a state is really a limiting condition. Further, since coherent structures exist on the larger scales, it is reasonable to assume the existence of similar structures on all scales larger than the dissipation scale. Second, the transition to turbulence does not occur through an infinite succession of instabilities, but after the appearance of relatively few instabilities, typically three or four. This has led to the postulate of a theoretical connection between strange-attractor theory and transition to turbulence. Third, intermittency in free turbulent shear layers indicates the presence of a thin, sharp interface between turbulent fluid and irrotational fluid. This finding leads to questions about whether such sharp interfaces can be represented as a diffusive effect. Finally, the recent discovery that coherent structures dominate flows which were previously believed to approach pure turbulence directly causes us to reconsider the basic assumptions in the classical theory of turbulence.

The search for new concepts of the nature of turbulence has centred on understanding the mechanisms of the transition to turbulence in several simple fluid flows. Shear flows generated by splitter-plate partitions (e.g. Brown & Roshko 1974; Browand & Weidman 1976; Roshko 1976) exhibit most of the troublesome intricacies associated with the transition and have properties that are relevant to practical applications. Both larger and smaller scales of chaotic fluid motion develop in these systems. Flow near the sharp trailing edge of the splitter plate, where the parallel free streams first

meet, may initially be laminar for even high Reynolds numbers, and several distinct transitions are easily discerned before the onset of an apparently fully turbulent shear layer. It is still quite difficult, however, to pinpoint at which stage in the flow the label 'turbulent' becomes applicable. Indeed, large-scale coherent structures have been found to dominate well downstream in flows which appear chaotic on smaller scales. By using similarity arguments, for example, we see that the splitter-plate flow is always dominated by ever larger coherent structures. Through flow-visualization experiments, a great deal of insight has been achieved into the exact mechanisms involved in the individual instabilities as well as some indication of the sequence of appearance of various scales of motion.

The shear layer generated by the splitter plate is subject to the Kelvin-Helmholtz instability. Small perturbations in the flow grow into nonlinear waves which break and roll up, transforming the original vorticity of the shear layer into isolated clumps. The primary wavelength generated by the instability is usually that of the fastest-growing mode for that particular geometry or of some impressed wavelength determined by boundary conditions or initial conditions. Further development of the shear layer proceeds through the pairing of vortex clumps, a process which may be repeated many times downstream. One of the effects of pairing is to generate subharmonics of the original unstable wavelength, but smaller-wavelength disturbances are created as well. These disparate wavelengths arise from at least two causes: imperfect pairing due to small fluctuations in the flow leaving an unpaired vortex which then merges with a previously formed pair (Browand & Winant 1973), and the generation of small-scale disturbances in the interaction of the cores of the two vorticity clumps (Zabusky 1981).

A number of experimental investigations have shown that the large spanwise coherent structures dominate the entrainment and mixing processes at the shear layers (Winant & Browand 1974; Brown & Roshko 1974; Dimotakis & Brown 1976; Breidenthal 1981). Fluid entrained from the free streams can be transported unmixed across the shear layer. When chemical reaction between the entrained fluids is possible, it takes place preferentially at the regions associated with the coherent structures. In many practical applications, such as combustion and chemical lasers, mixing layers are important and it is extremely helpful to understand mechanisms by which mixing can be enhanced or retarded.

Recent splitter-plate experiments by Koochesfahani *et al.* (1983) show that more high-speed fluid than low-speed fluid is entrained in the coherent structures. The experimental work of Konrad (1976) suggested that the entrainment at the shear layer is not necessarily symmetric. Broadwell & Breidenthal (1982) developed a simple mixing model which may explain the observed results. This asymmetry is not predicted by models based on gradient transport and eddy diffusivity. It has also not been noted in spectral simulations of unsteady shear flows with periodic boundary conditions (Riley & Metcalfe 1980), or in previous simulations of the splitter-plate geometry using either vortex (Ashurst (1979) or finite-difference (Davis & Moore 1985) methods.

In the work presented below, we describe numerical simulations of two-dimensional shear flows of a splitter-plate geometry. Our goal is to produce accurate enough calculations of the time evolution of the major physical quantities so that we can analyse the flow behaviour and test concepts of the transition to turbulence. We are interested in the initial transient behaviour, the resulting unsteady pattern of structures, and the symmetry properties of the composition of their associated mixing layers.

### 3. The numerical model

#### 3.1. Flux-corrected transport

The FAST2D simulation model was used to perform the shear-flow calculations described below. This program solves the inviscid, compressible, time-dependent, conservation equations for mass, momentum and energy. Algorithms describing gravity, molecular and thermal diffusion, and chemical reactions with energy release are also a part of the model, but were not used in the calculations presented here. The algorithms describing the various physical processes are coupled by timestep splitting so the corresponding physical effects can be turned on or off independently as required by the particular problem being studied. No subgrid turbulence phenomenology has been included at this stage of development of the model.

The conservation equations are solved using Flux-Corrected Transport (Boris & Book 1976), a nonlinear, monotone, finite-difference technique which conserves mass, momentum and energy and preserves the physical positivity property of fluids. FCT is particularly useful in problems where sharp discontinuities arise and are maintained throughout the calculations. These discontinuities may be shocks or contact surfaces, or, as in the case presented in this paper, interfaces in material density. FCT adds linear velocity-dependent diffusion to a high-order algorithm during convective transport. This prevents dispersive ripples from arising, and thus ensures that all conserved quantities remain monotone and positive. Fourth-order accuracy is maintained by subtracting out this added diffusion during a second nonlinear antidiffusion stage of the algorithm in regions where it is not needed to preserve monotonicity. The algorithm has been used extensively in one-, two- and three-dimensional flows (e.g. Oran *et al.* 1982; Picone *et al.* 1983; Kailasanath & Oran 1985*a,b*; Fyfe *et al.* 1985).

Another important feature of FCT is its ability to separate grid motions from the fluid flow. This allows us to use variably spaced grids as well as moving adaptive grids (Book *et al.* 1980; Oran *et al.* 1982). Figure 1 is an example of a convergence test that was done for the calculation of a shock which underwent transition to a detonation. A shock propagating in a tube containing a mixture of hydrogen, oxygen, and argon reflects from a rigid wall. Upon reflection, the temperature and pressure are raised high enough to initiate chemical reactions. The chemical reactions occur first near the wall, where a reaction wave eventually forms. The reaction wave overtakes the reflected shock and the result is a propagating detonation. This problem was studied computationally using FCT coupled to a chemical-kinetics model, and the results were compared with experimental shock-tube data (Oran *et al.* 1982). Figure 1 shows a series of resolution tests for one of the cases studied. The first calculation, (*a*), used a uniform, stationary grid with a cell spacing of 0.07 cm. The second and third calculations, (*b*) and (*c*), both used moving, variably spaced grids with different minimum spacing around the detonation front. This is a difficult problem to formulate because the grid was both variable and moving. However, the cost benefits of using such flexible grids are substantial. Resolution tests for multidimensional versions of this model with variably spaced and moving grids, have been reported by, e.g., Book *et al.* (1980) and Kailasanath & Oran (1985*a, b*).

The particular version of FCT used here is JPBFCF, which is similar to ETBFCT (Boris 1976*a*). This routine solves the one-dimensional continuity equation in Cartesian, cylindrical, spherical or generalized nozzle geometries, depending on the value of a logical switch. Since the algorithm is one-dimensional, timestep splitting in the various directions is used to construct two- and three-dimensional codes. The

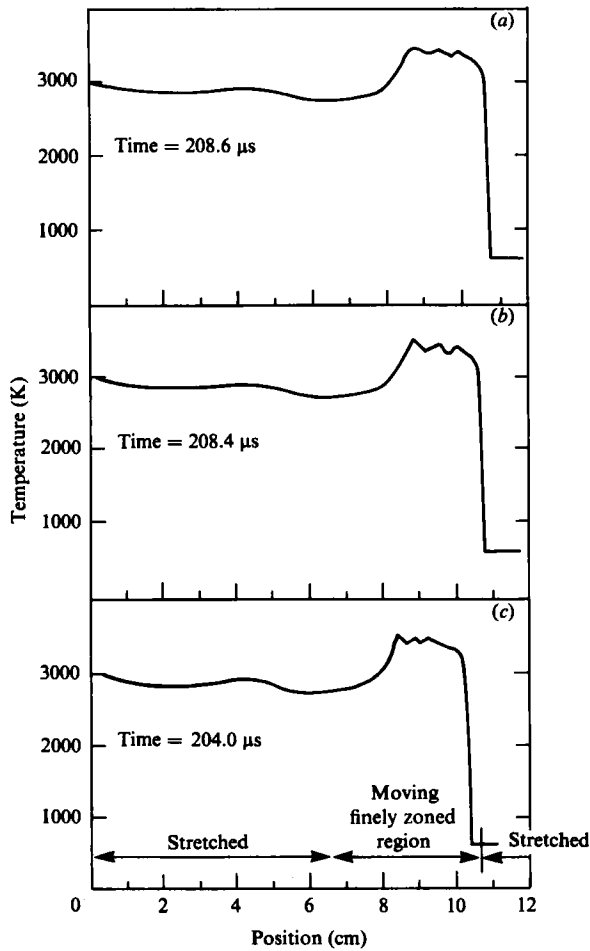


FIGURE 1. Resolution tests of a chemically reactive Flux-Corrected Transport calculation. Temperature versus position for a propagating detonation for three choices of computational grid: (a) uniform grid with spacing 0.07 cm; (b) variably spaced grid with minimum spacing around the detonation front of 0.07 cm, maximum spacing far from the front of 2.00 cm; (c) variably spaced grid as in (b) with minimum spacing of 0.035 cm and maximum spacing of 2.00 cm. Stretched and finely gridded regions are marked in (c).

two-dimensional Cartesian calculations described below were performed with the general code with the gravity, diffusion, chemistry, and energy-release options not used (discussed elsewhere by Oran & Boris 1981).

### 3.2. Computational grid

The computational grid was set up initially in the calculations and then held fixed in time. A typical grid is shown in figure 2(a). Finely spaced cells clustered around the centreline where the instability first occurs and the coherent structures form. The splitter plate is on the centreline and its trailing edge is at  $Y = 2.0$  cm. The  $Y$ -direction is well resolved near the centreline. The velocity of the lower stream ( $V_l$ ) is always considerably larger than that of the upper stream ( $V_s$ ). As the large spanwise vortices propagate downstream, they merge and grow. The idea is to have the larger computational cells (further downstream and further from the centreline) resolve the larger coherent structures, and the smaller cells resolve the smaller structures.

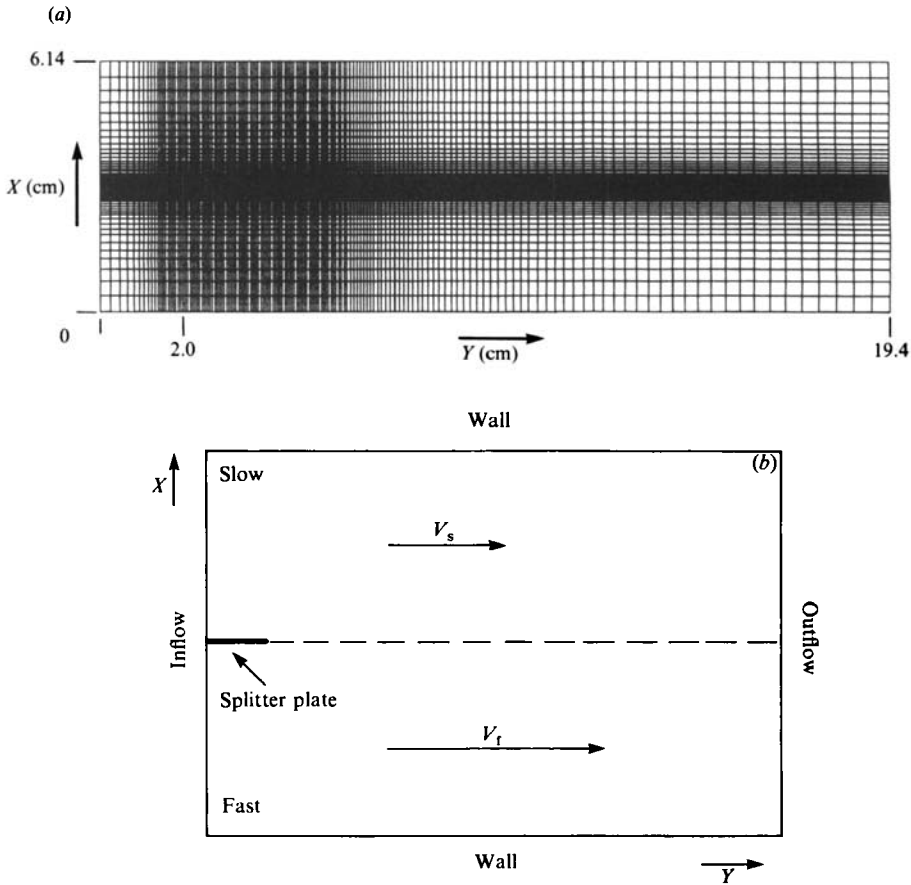


FIGURE 2. (a) Sample computational grid used in the calculations. Minimum  $X$ -spacing = 0.024, maximum  $X$ -spacing = 0.24, minimum  $Y$ -spacing = 0.060, maximum  $Y$ -spacing (left) = 0.24, maximum  $Y$ -spacing (right) = 0.46. The splitter plate is on the centreline, with its trailing edge located at  $Y = 2.0$  cm. (b) Schematic diagram showing the initial and boundary conditions for the splitter-plate simulation.

Grid spacing was varied in different calculations to (i) check the effects of resolution, (ii) test the implementations of various boundary-condition algorithms, and (iii) test the effects of physically different boundaries. Maxima of 100 cells across the mixing layer ( $X$ -direction) and 170 cells in the streamwise direction ( $Y$ -direction) were used. The first 20 cells in the  $Y$ -direction were in the region behind the tip of the splitter plate. The mesh spacing varied in the range 0.024–0.24 cm in the  $X$ -direction, and 0.06–0.46 cm in the  $Y$ -direction. In general, the spacing should not stretch or compress more than 20–30% from cell to cell.

Typical convergence tests varied the spacing in both directions by  $\pm 50\%$ . The observed differences in the calculations made minor differences in the quantitative results, and no differences in the qualitative observations. In an Eulerian finite-difference calculation, varying the grid spacing is the most rigorous test of a computational model. The results presented in §4 have been calculated on a  $60 \times 150$  grid. A discussion of the sensitivity of the results to the location of the boundaries and the boundary conditions used in the calculations is given at the end of §4.

### 3.3. Boundary conditions

As shown in figure 2(b), the top and the bottom of the computational region are perfectly reflecting hard walls. These boundary conditions are implemented by assuming that the  $X$ -component of the velocity at the guard cell is equal to minus the  $X$ -component of the velocity at the first cell inside the domain. These types of boundary conditions are also imposed at the splitter plate to ensure that there is no flux of material across its surface. Assuming a free-slip condition at the walls and at the splitter plate is a first approximation that we use in this inviscid calculation. It is unlikely that the effects of boundary layers at the walls would considerably affect the calculated flowfield. In particular, the location and presence of the walls does not significantly affect the calculated asymmetries described below (see §4.3).

Fluid viscosity and boundary layers are important only at the splitter plate and at the initial stage in which the Kelvin–Helmholtz instability is triggered. The subsequent instability mechanism is essentially an inviscid phenomenon, and the effect of viscosity is only to damp the process. The boundary layers (not accounted for in the calculations) provide a lengthscale, namely the initial thickness  $\theta_0$  of the shear layer. Because of viscous diffusion, the laminar streams should give rise to a wake-like velocity profile immediately downstream of the trailing edge of the splitter plate. The profile then gradually relaxes to a shear-layer velocity distribution, with the necessary inflexion point for the flow to become unstable with respect to small wavy disturbances (Rayleigh 1880).

In our numerical model we start out with a step-function velocity profile across the shear layer. This profile smooths out during the initial integration cycles, and relaxes to a shear-layer profile with an effective non-zero initial thickness  $\theta'_0$ . The experiments at high Reynolds numbers indicate that the spatially growing instabilities are only affected by the Strouhal number  $St = f\theta/V_0$ , where  $f$  is the most amplified frequency,  $\theta$  is the shear-layer thickness and  $V_0$  the mean free-stream velocity (Freythuth 1966; see also, e.g., Ho & Huang 1982). Because these characteristic flow parameters can be effectively reduced to  $St$  alone, we can expect that this inviscid two-dimensional treatment can provide a reasonable approximation to many of the features of the flow dynamics for high Reynolds number. The value of  $\theta'_0$  essentially affects only the frequency of the most unstable mode in the initial region of the mixing layers. Typical estimates for the Strouhal number, at the initial stages of our simulations, where  $\theta'_0$  is equal to one cell in the cross-stream direction, give  $St = 0.040$ . This is in reasonable agreement with the value  $St_n = 0.032 \pm 0.002$  for the most unstable mode from linear inviscid stability theory (Ho & Huerre 1984).

The fundamental difficulty when solving problems with outflow-boundary conditions is that information about the flow beyond the computational mesh is required to make the fluid near the boundaries behave properly. This problem is generally handled by using guard cells. Guard cells are just outside the computational region, and are not actually part of the calculation. They are used to tell the boundary cells how the outside world is behaving. The simplest model of outflow in guard cells is to say that the momentum, energy, and density do not change, i.e. there is effectively zero gradient. This causes problems in extended calculations since it does not provide a way for the solutions to relax to background conditions.

An outflow-boundary algorithm was developed to use with the FCT algorithm described in §3.1. This algorithm defines the values of quantities at the guard cell from a zeroth-order extrapolation of the value at the boundary cell. In addition, it assumes that there is a slow local relaxation outside the mesh towards the known

ambient value. The strong nonlinear stabilizing properties of the FCT method appear to eliminate instabilities which occur in other non-local methods when low-order extrapolations are used for specifying boundary conditions (Turkel 1980). Previous tests (Boris *et al.* 1985) have suggested this as a simple, yet effective, approach to the outflow-boundary conditions. Such an expression is expected to be an approximation to the lowest-order terms in an asymptotic expansion, valid for times short compared to a sonic transit time of the system.

For two-dimensional incompressible calculations, Davis & Moore (1985) specify background values and use zero-gradient conditions at infinite distances from the computational region. Their boundary conditions are implemented by mapping the infinite physical space into a finite computational domain. Their approach to outflow has important elements in common with the method used here. Both methods stretch the mesh to get the boundary far from the region of interest.

The algorithm is implemented by assuming that the pressure in the guard cell is extrapolated from the boundary cell but relaxes to a prespecified ambient value. Specifically, if  $Y$  is the streamwise (outflow) direction,

$$P_g = P_n + \frac{Y_g - Y_n}{Y_g - Y_s} (P_{amb} - P_n), \quad (1)$$

where  $P_g$  is the guard-cell pressure,  $P_{amb}$  the ambient pressure,  $P_n$  is the boundary pressure and  $Y_g$ ,  $Y_n$  and  $Y_s$  correspond to the positions of the guard cell, the boundary cell and the cell at the edge of the splitter plate, respectively. This expression is derived by assuming that the pressure reaches its ambient value at  $Y = \infty$ , and  $P_g$  is then obtained by linearly interpolating (in the variable  $1/(Y - Y_s)$ ) between  $P_n$  and  $P_{amb}$ . This is a one-dimensional first approximation to the correct outflow-boundary condition.

The density and momenta are extrapolated according to

$$\rho_g = \rho_n, \quad (2)$$

$$(\rho V_x)_g = (\rho V_x)_n, \quad (3)$$

$$(\rho V_y)_g = (\rho V_y)_n. \quad (4)$$

Further improvements for  $P_g$  are possible by considering higher-order interpolation schemes, i.e. by including the information on the pressure at other cells in the domain in addition to that at the boundary cells. In particular, it might be useful to include an explicit dependence on physical parameters of the problem such as the separation between the walls, the size and rate of flow of the structures and the local speed of sound. This requires further physical assumptions about conditions outside of the computational domain in the downstream direction.

In our preliminary calculations, we used inflow-boundary conditions which specified constant values of the mass, momentum and energy of the inflowing gas. Also, the inflow boundary was at the tip of the splitter plate. These conditions, however, did not correctly provide the feedback between the fluid just entering the computational domain and the disturbances created downstream by the Kelvin-Helmholtz roll-ups and vortex merging. Pressure pulses from downstream disturbances create small transverse flows at the trailing edge of the splitter plate. These pulses re-initiate the instability and lead to the next coherent vortex roll-up. When the inflow pressure was held equal to the ambient pressure, the first vortex structures formed very far downstream. They eventually flowed off the computational domain,

and the instability appeared to die out. The apparent reason for this is that the pressure perturbations arriving at the inflow boundary were cancelled by the non-physical condition which kept the inflow pressure constant. A more physically reasonable treatment of the inflow response to pressure fluctuations was required.

The inflow-boundary conditions we use now specify the inflow density and velocity, and then use a zero-slope condition on the pressure at the inflow boundary to derive the energy. This algorithm allows pressure differences between the top and bottom streams to generate transverse flows. In addition, a short inflow plenum is modelled by including the 2.0 cm region behind the end of the splitter plate in the computational domain, as shown in figure 2(a).

With a fluctuating inflow-pressure condition, it is important to relax the outflow pressure toward an ambient value. This is because a base pressure for the system has to be specified in compressible calculations when the value of the inflow pressure is allowed to vary. Relaxation of the density and momentum towards their ambient values is less important on outflow because these values are given at the inflow boundary. The long-time values of all the variables must be available to the solution from the beginning to prevent secular deviation of the calculated flow.

#### 4. Splitter-plate simulations

As shown in figure 2(b), two coflowing streams of air are initially separated by a thin plate and then enter a long chamber. The simulations are initialized by assuming that both gas streams have the same initial pressure (1 atm) and temperature (298 K), and have initial uniform velocities  $V_f$  and  $V_s$ . The values considered for  $V_f$  and  $V_s$  ranged from  $1.0 \times 10^4$  to  $2.0 \times 10^4$  cm/s, and from 0 to  $4.0 \times 10^3$  cm/s, respectively. The range  $V_s/V_f$  of 0–0.2 was studied. Since the velocity of sound in this mixture is typically of the order of  $3.5 \times 10^4$  cm/s, the flows were subsonic and hence virtually incompressible. The FCT algorithm used to describe the convection flow, however, is fully compressible, so sound waves are resolved in the system and acoustic delay times for pressure waves are properly accounted for.

The small perturbation which initiates the transition from laminar to turbulent flow occurs at the first time step of the calculation. It is analogous to using a delta-function perturbation at the centre in a periodic simulation of two equal and opposite streams. The perturbation generates small pressure gradients and diffuses vorticity at the shear layer, near the edge of the splitter plate. The initial step-function profile for the downstream velocity is smoothed out after the first few convection cycles. As a consequence, the initially uniform pressure develops a small gradient across the thickening shear layer in the region close to the edge of the splitter plate where the free streams meet. This disturbance moves downstream as the integration proceeds, generating the transverse flows which trigger the instability.

##### 4.1. Transition from laminar to turbulent flow

Figures 3–7 show the development of the flow for the case in which  $V_f = 1.0 \times 10^4$  cm/s and  $V_s = 2.0 \times 10^3$  cm/s (i.e.  $V_s/V_f = 0.2$ ). The time evolution of the flow is shown through sequences of isovorticity and number-density ratio ( $R$ ) contour plots, where

$$R = \frac{N^f}{N^f + N^s}. \quad (5)$$

The  $N^f$  and  $N^s$  are the number densities corresponding to the faster and slower inflowing streams, respectively.  $R$  varies between 0 and 1, which corresponds to 100 %

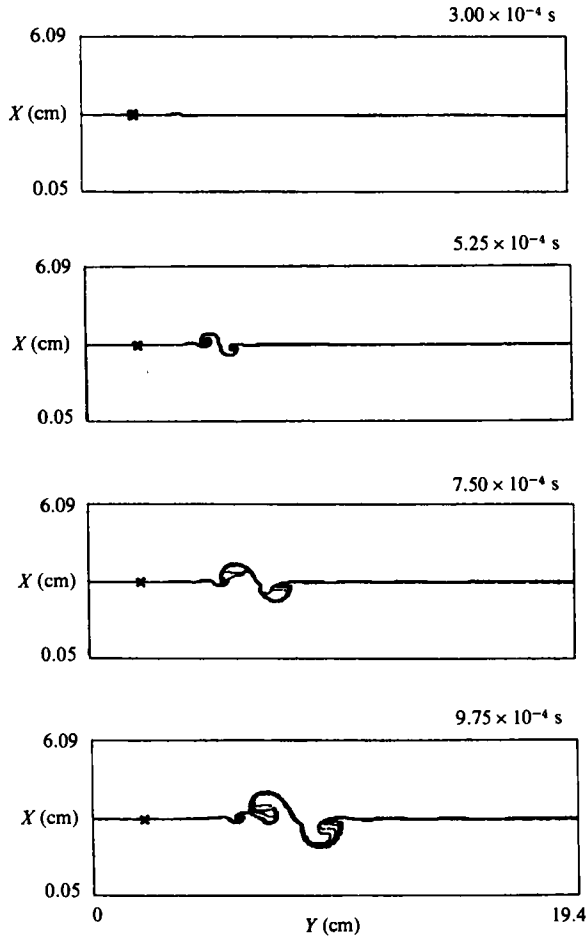


FIGURE 3. Typical initial stages in the development of the Kelvin-Helmholtz unstable flow for the splitter-plate problem. The right edge of the splitter plate is located at  $x$  on the centreline.  $V_f = 1.0 \times 10^4$  cm/s,  $V_s = 2.0 \times 10^3$  cm/s. Contours of the mixing ratio  $R$ , as defined by (5), for 0.3, 0.4, 0.5, 0.6, and 0.7.

of the slower stream or 100% of the faster stream, respectively. The choice of negative isovorticity contours in figures 4 and 7 gives the best flow visualization.

In figures 3 and 5,  $R$  is contoured in the interval 0.3–0.7. This particular choice of contour levels is useful for describing the mixing. The transition from a uniform shear flow first appears as a pair of vortices forming just ahead of the tip of the plate, shown at 0.525 ms in figure 3. As this pair travels downstream, it grows steadily owing to the vorticity which is being fed into it from both directions. In addition, smaller structures are entrained by the roll-up on the side of the splitter plate. As the system evolves, the smaller structures have more time to grow before they are engulfed. The last panel, at 0.975 ms, shows one of these small structures, now a vortex, being shed and merging with the large vortex.

The isovorticity contours in figure 4 show the shear layer breaking up. New vorticity clumps form and subsequently pair with the leading vortex. A relation exists between the growth of the leading vortex, through the pairing process, and the rate at which new vortices are shed. Pressure disturbances are generated by the fluid

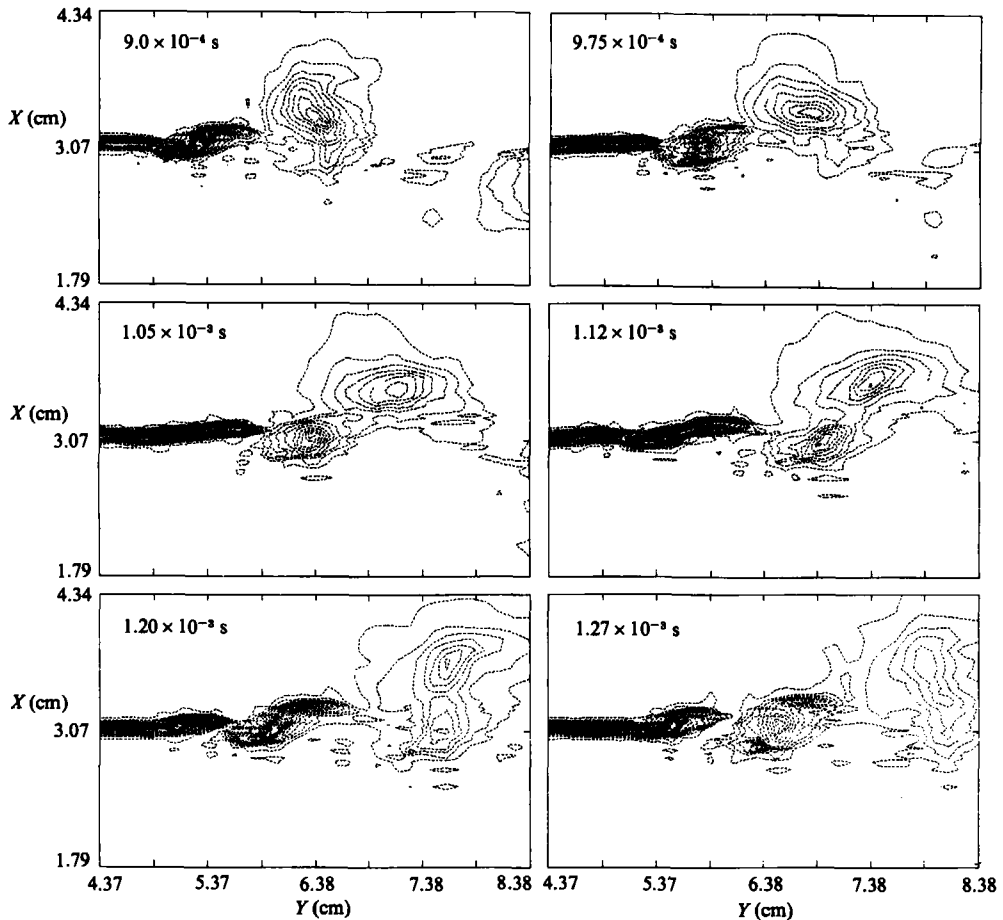


FIGURE 4. Sequence of isovorticity contours for the initial stages in the development of the Kelvin-Helmholtz unstable flow for the splitter-plate problem. Contour levels are equally spaced, with an interval of  $-6.0 \times 10^8 \text{ s}^{-1}$ . The vorticity at the outermost contour is  $-2.0 \times 10^8 \text{ s}^{-1}$ , decreasing to a minimum of  $-9.8 \times 10^4 \text{ s}^{-1}$  near the tip of the splitter plate.

accelerations caused by downstream roll-ups and mergings. These disturbances can reinitiate the instabilities close to the trailing edge of the splitter plate. The choice of the inflow boundary condition was crucial in allowing for this physical feedback mechanism to occur. This concept was tested by damping the acoustic pulses reaching the inflow boundary. This was the initial inflow-boundary condition described above in §3, where the pressure at the tip of the splitter plate was set equal to the ambient pressure.

Figure 5 is a continuation of the same calculation at later times, from 0.975 to 2.620 ms. Small vortices are shed at about 1.0–1.6 cm from the tip of the splitter plate. Larger vortices have moved downstream. The more frequent mergings with the leading vortex, like the one seen in figure 4, are responsible for its faster growth. This growth becomes more pronounced as the large structure moves into the coarser part of the computational grid (say for  $t > 2.0$  ms), where it is somewhat spread out by increased numerical diffusion. Pairings between the newly shed vortices are also possible now, as they become more separated from the leading vortex. By 2.62 ms,

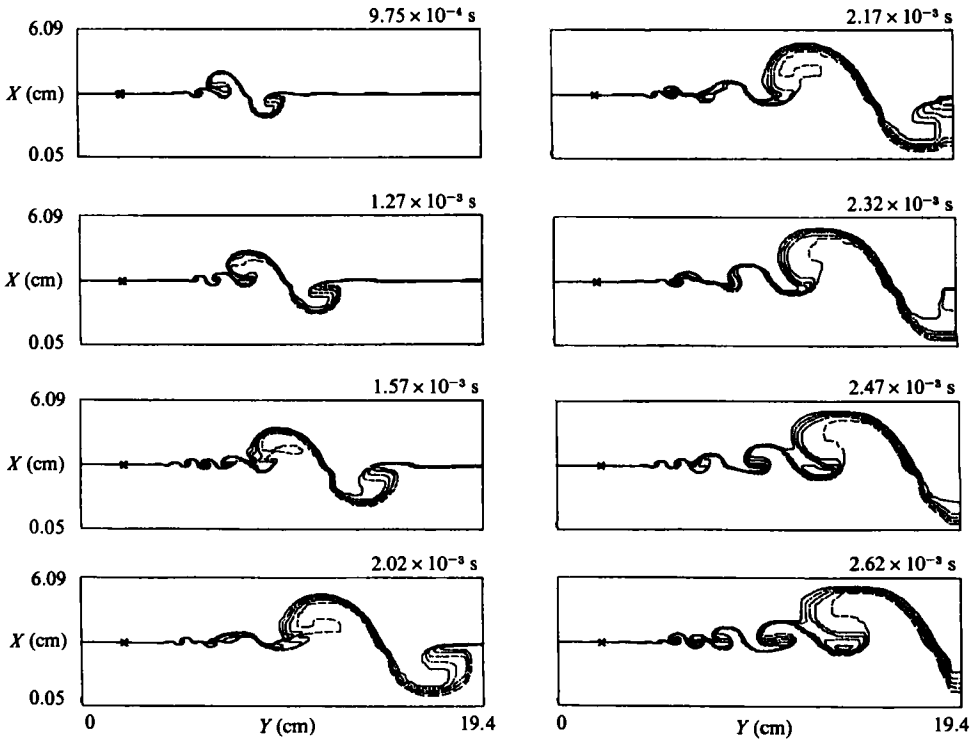


FIGURE 5. Contours of  $R$ , as in figure 3, for later stages in the development of the flow.

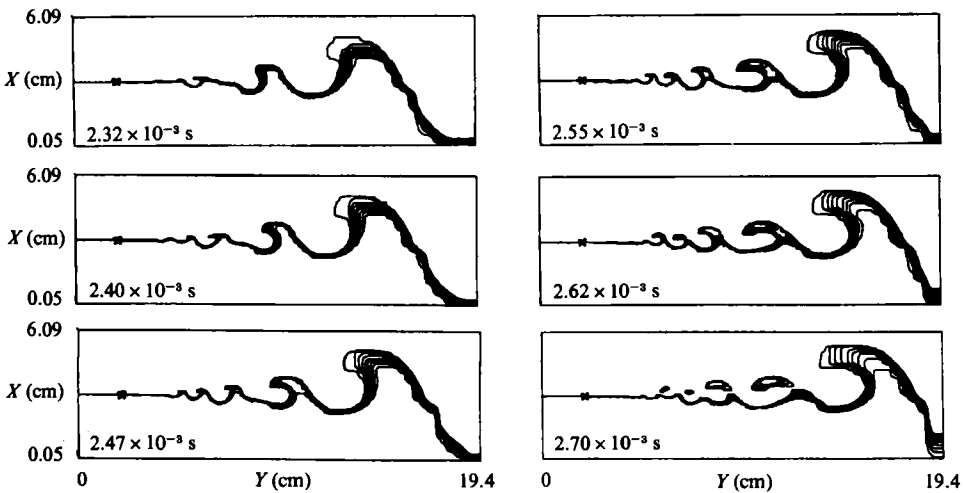


FIGURE 6. Contours for equally spaced values of  $R$  in the interval 0.70–0.97, for later stages in the development of the flow in the case of figure 3.

the last panel in figure 5, merging vortices move off the right edge of the computational system and unperturbed fluid moves in on the left.

Figure 6 shows contours of  $R$  in the range 0.70–0.97. This choice of contour levels emphasizes the portions of the faster fluid which are transported largely unmixed across the shear layer. Isovorticity contours corresponding to these frames are shown

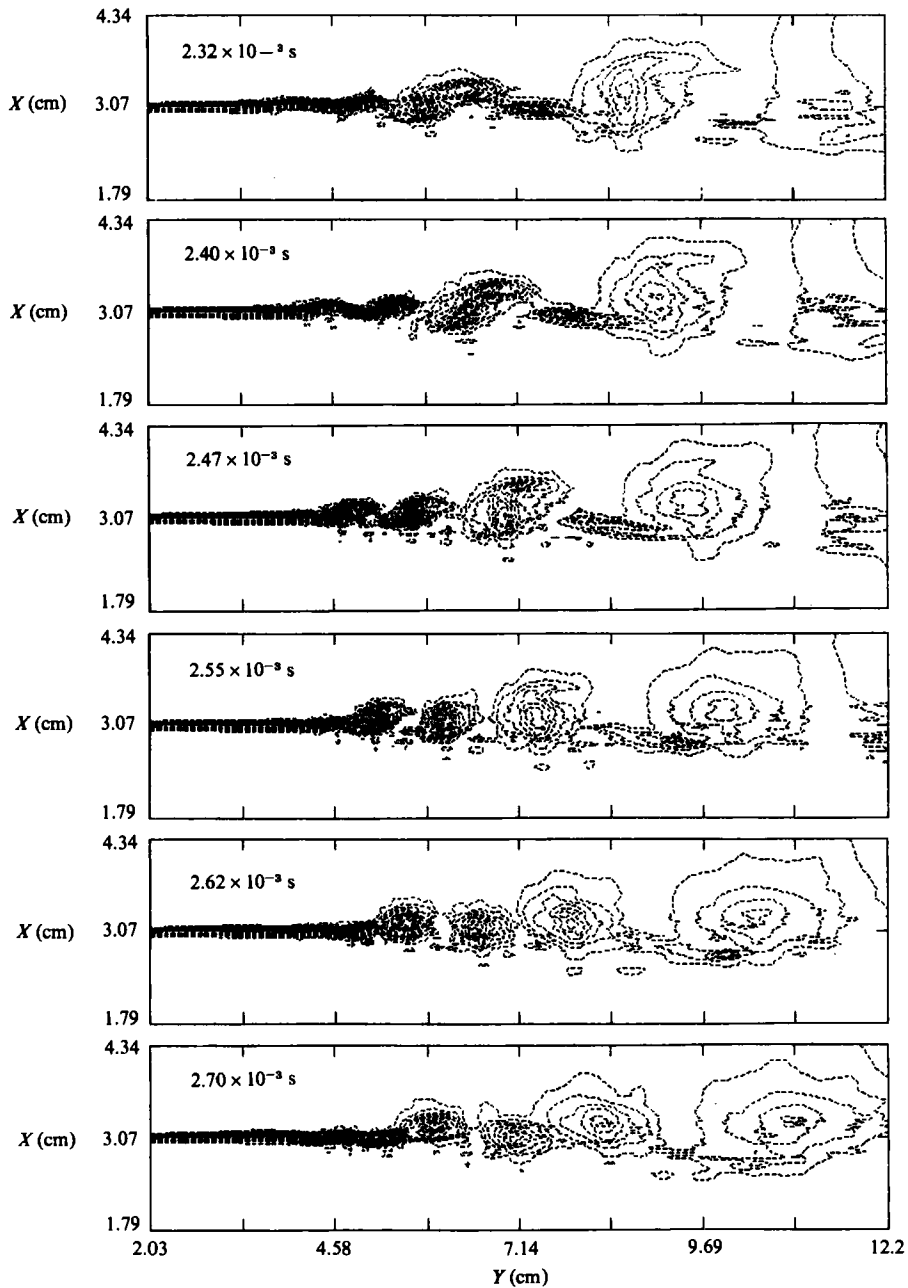


FIGURE 7. Isovorticity contours, for later stages in the development of the flow in the case of figure 3. Isovorticity levels as in figure 4.

in figure 7. We see that the growth pattern of the structures appears to follow a similarity law. This is consistent with the flow having a lengthscale which increases downstream proportionally to the distance from an origin of similarity located just ahead of the edge of the splitter plate. By the last frame at 2.62 ms (see also figure 5), a spectrum of modes is seen suggesting a snapshot from an experimental flow visualization. As can be seen from the figures, some asymmetry exists in the similarity

pattern. Structures penetrate further from the centreline on the low-speed side. This deflection is also observed in the experiments (see e.g. the shadowgraphs in Brown & Roshko 1974 and in Konrad 1976).

#### 4.2. Asymmetries in the composition of the mixing layers

Experiments by Koochesfahani *et al.* (1983) show that there is more high-speed than low-speed material entrained and mixed in the coherent structures. These experiments investigated the composition of the mixing layers by using a dilute acid solution and a dilute base solution for each of the free streams, and examining the extent of the titration process. A pH-sensitive fluorescent dye was premixed with the acid solution. Then laser-induced fluorescence was used to monitor the local chemical environment at the shear layer and in the mixed region between the two streams. The amount of chemical product was estimated as a function of the amount of (fluorescent) fluid having a pH above the fluorescence threshold. Two identical experiments were performed in which the faster stream was alternately acidic or basic. Comparison of the results indicated that the amount of product was larger by two orders of magnitude in the case in which the faster stream was basic. This suggests that the entrainment at the shear layer is asymmetric, with an excess of higher-speed fluid in the composition of the mixing layers.

In order to evaluate the mixing asymmetries in our calculations, we have simulated this fluorescence diagnostic. We assume that the streams of air are prepared as in the experiment, namely that one is a dilute 'acid' solution carrying a pH-sensitive dye which 'fluoresces' when the pH is above a certain threshold, and the other is 'basic'. The acid (plus dye) and base additives to the streams of gas are small enough that convection is not perturbed by their presence.

We then define a fluorescence intensity  $I$ . Let streams  $s$  and  $f$  be the acid and base streams, respectively. Also let the streams have an equivalence ratio such that 1 part of the base stream is required to neutralize 1 part of the acid stream and elevate the local pH above the dye threshold. Then, the fluorescence intensity  $I_{ij}^{fs}$  at cell  $(i, j)$  is

$$I_{ij}^{fs} = \begin{cases} N_{ij}^s/N_0, & \text{if } N_{ij}^f > N_{ij}^s, \\ 0, & \text{if } N_{ij}^f < N_{ij}^s, \end{cases} \quad (6)$$

where  $N_0$  is a normalization constant. The index  $i$  refers to the cross-stream ( $X$ ) direction and  $j$  refers to the streamwise ( $Y$ ) direction. In addition, we assume that a fluorescent portion of the fluid has an excess of base, as in the experiment, and that the intensity is proportional to the amount of dye in the cell. This ensures that the intensity decreases to zero in the pure base stream and provides a very simple physical cutoff defining the mixing layers. Analogously, we define an intensity  $I_{ij}^{sf}$  corresponding to the reversed case in which streams  $f$  and  $s$  correspond to the (acid + dye) and base solutions, respectively. Both intensities can then be calculated from the same computed data.

By comparing  $I^{fs}$  and  $I^{sf}$ , we can evaluate the mixing asymmetry at the shear layer in terms similar to those used in the experiment. A smooth exponential interpolation was made between 0 and  $N_{ij}^s/N_0$  in defining  $I_{ij}^{fs}$  for  $N_{ij}^f$  in the range  $0.95 \times N_{ij}^s$  to  $1.0 \times N_{ij}^s$ . The corresponding interpolation was made for  $I_{ij}^{sf}$ . The normalization constant  $N_0$  was defined as  $N_0 = P/k_B T$ , where  $P$  and  $T$  are the values of the initial uniform pressure and temperature, and  $k_B$  is Boltzmann's constant. With this definition, the fluorescence intensities are between 0 and 0.5. Some representative cases are shown in figures 8–10 for  $V_s/V_f = 0, 0.1, \text{ and } 0.2$ . The first case corresponds

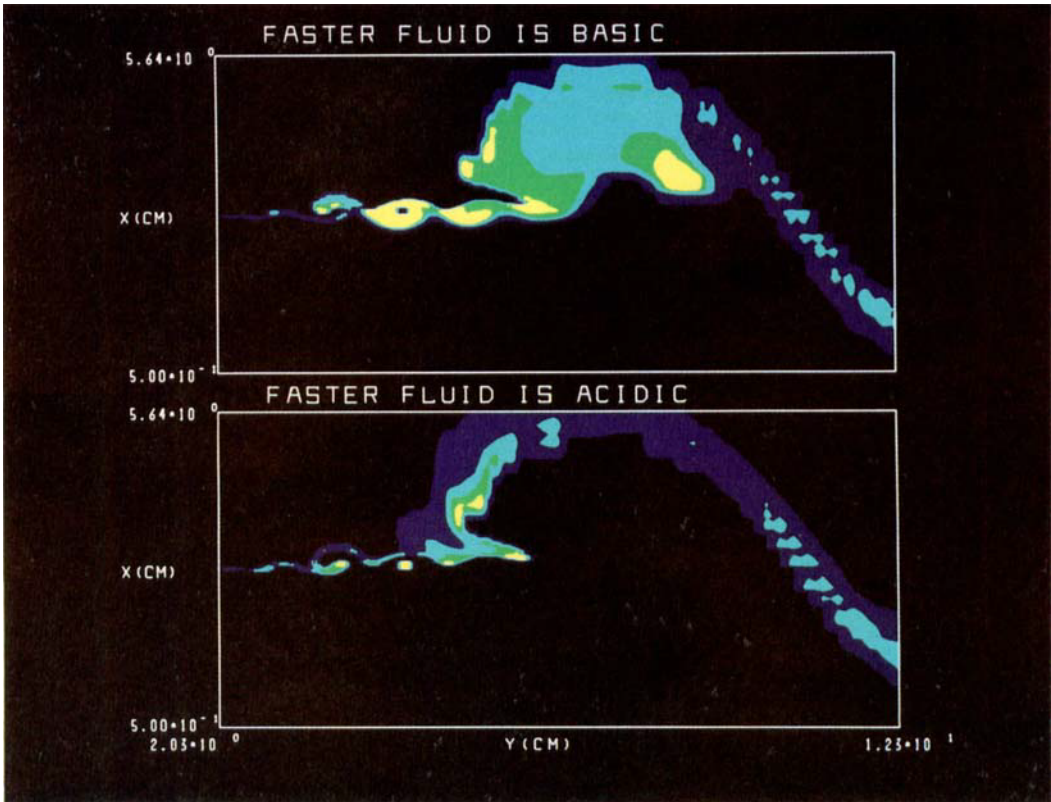


FIGURE 8. Contours of the mixing intensity  $I$ , as defined by (6), for  $V_s/V_f = 0$  with  $V_f = 2.0 \times 10^4$  cm/s. Step =  $3.00 \times 10^3$ , Time =  $9.00 \times 10^{-4}$  s. Dark blue:  $0.005 < I < 0.125$ ; Turquoise:  $0.125 < I < 0.250$ ; Green:  $0.250 < I < 0.375$ ; Yellow:  $0.375 < I < 0.500$ .

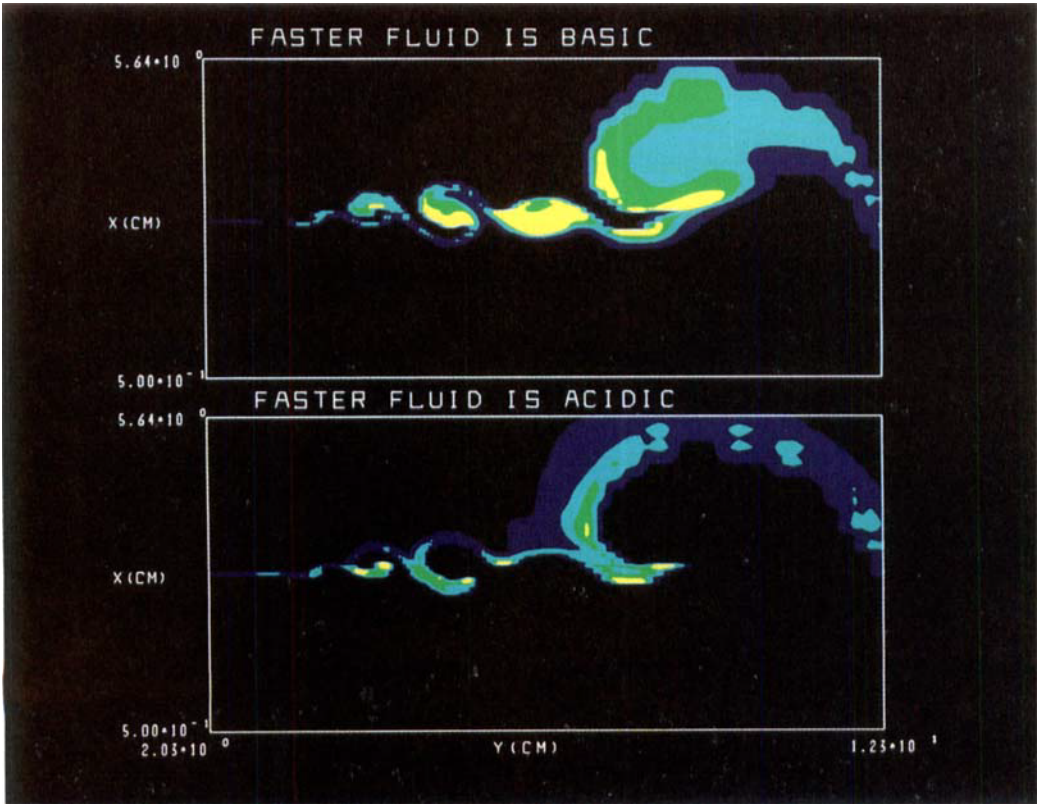


FIGURE 9. Contours of  $I$ , for  $V_s/V_f = 0.1$ , and  $V_f = 2.0 \times 10^4$  cm/s. Step =  $3.20 \times 10^3$ , Time =  $9.60 \times 10^{-4}$ s. Key given in figure 8.

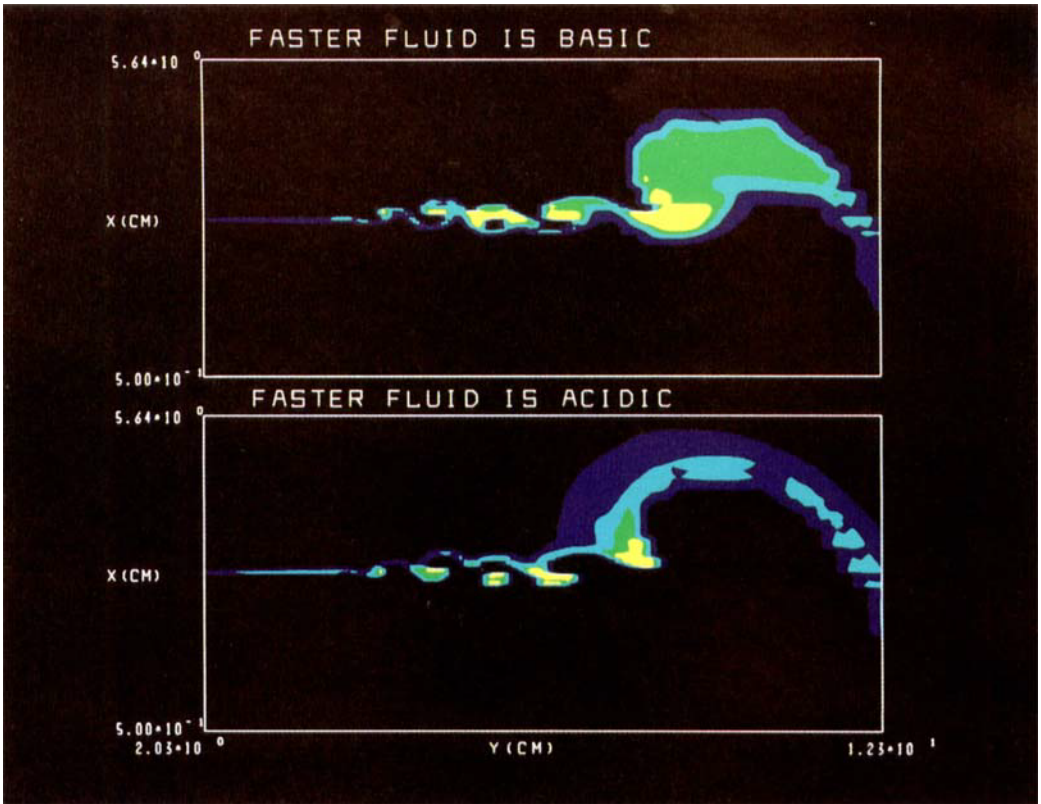


FIGURE 10. Contours of  $I$ , for  $V_s/V_f = 0.2$ , and  $V_f = 1.0 \times 10^4$  cm/s. Step =  $5.50 \times 10^8$ , Time =  $1.65 \times 10^{-3}$ s. Key given in figure 8.

to a quiescent upper stream. The coloured regions indicate the locations where the intensities are appreciably different from zero, as determined by the requirement  $I > 0.005$ .

Figures 8–10 (plates 1–3) show that, as the velocity ratio increases, the instability appears closer to the edge of the splitter plate, and the structures grow faster. This result is expected, since the growth rates of the Kelvin–Helmholtz instability increase with the velocity difference. We can roughly define fluorescent regions as those regions covered by the lighter colours, i.e. those for which  $I$  is greater than a threshold value  $I_0 = 0.125$ , equal to 25% of the maximum attainable value. The figures show that the fluorescent area is greater when the faster stream is basic and the dye is in the slower acid stream. This means that the mixing layer has more of the faster than of the slower fluid.

In order to get a global measure of the asymmetry, we consider a ratio of effective fluorescent areas,  $Q(Y)$ , defined by

$$Q(Y) = \frac{\sum_{j=J_0}^J \sum_{i=1}^{N_x} I_{ij}^{fs} A_{ij}}{\sum_{j=J_0}^J \sum_{i=1}^{N_x} I_{ij}^{sf} A_{ij}}. \quad (7)$$

The sum over the index  $i$  is in the cross-stream  $X$ -direction and  $N_x$  is the number of cells in that direction. The sum over the index  $j$  extends over computational cells from the tip of the splitter plate, at location  $Y_0$ , cell  $J_0$  to a cut-off distance  $Y$  at cell  $J$ . The quantity  $A_{ij}$  is the area of the cell  $(i, j)$ .

The numerator and denominator in (7) correspond, respectively, to the fluorescent areas for the fs (base in the faster fluid, acid + dye in the slower fluid) and sf (acid + dye in the faster fluid and base in the slower fluid) flow configurations. Then, a mixing region of length  $(Y - Y_0)$  contains more of the faster fluid if  $Q(Y)$  is greater than 1.0. The average magnitude of  $(Q - 1.0)$  in the interval  $(Y_0, Y)$  considered gives a measure of the mixing asymmetry. Figure 11 shows  $Q(Y)$  as a function of  $Y$  for two cases,  $V_s/V_f = 0.1$  and 0.2, with  $V_f = 2 \times 10^4$  cm/s at 0.9 ms. This figure also shows that the mixing asymmetry increases as the ratio of free-stream velocities increases.

#### 4.3. The effects of boundaries on the mixing asymmetry

We performed a number of tests to evaluate the sensitivity of the calculations to the location of the boundaries and to different forms of outflow-boundary conditions. Our studies indicated that the results were not particularly sensitive to these kinds of variations. Some representative results involving rather significant changes are shown below in figures 12 and 13.

To test the effects of the location of the boundaries, we added computational cells above and below the splitter plate in the cross-stream direction, and at the outflow boundary in the streamwise direction. Figure 12 shows the ratio of fluorescent areas,  $Q$ , for two different-sized computational regions for the case in which  $V_s/V_f = 0.1$  and  $V_f = 2.0 \times 10^4$  cm/s, at 0.960 ms. The smaller region is the  $6.13 \times 19.44$  cm<sup>2</sup> considered before, and the other is a larger  $22.30 \times 24.9$  cm<sup>2</sup> domain. The shapes and exact locations of the maxima and minima of the curves are somewhat different since the curves are not for physically identical problems. However, the general features and, in particular, the asymmetry patterns are essentially the same.

In figure 13 we show the sensitivity of the results to changes in the outflow-boundary condition. We compare the curves of  $Q$  for two different outflow-boundary conditions in the case where  $V_s/V_f = 0.2$ ,  $V_f = 1.0 \times 10^4$  cm/s, at 1.725 ms. The solid

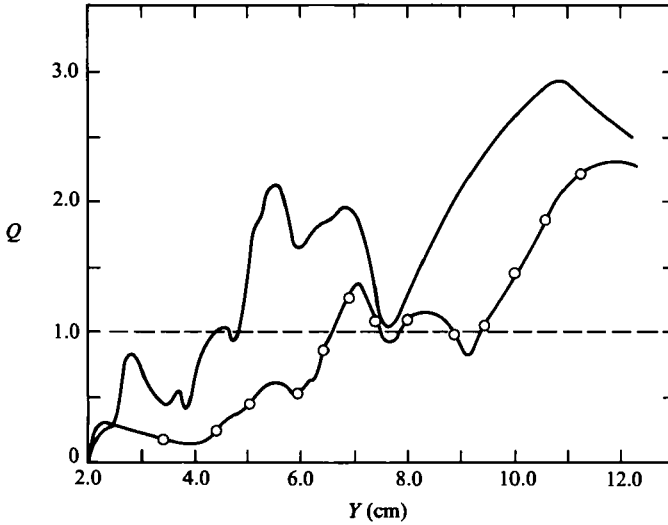


FIGURE 11. Ratio of fluorescent areas as a function of the streamwise direction at 0.9 ms, for  $V_f = 2.0 \times 10^4$  cm/s; solid line:  $V_s/V_f = 0.1$ , solid line with circles:  $V_s/V_f = 0.2$ .

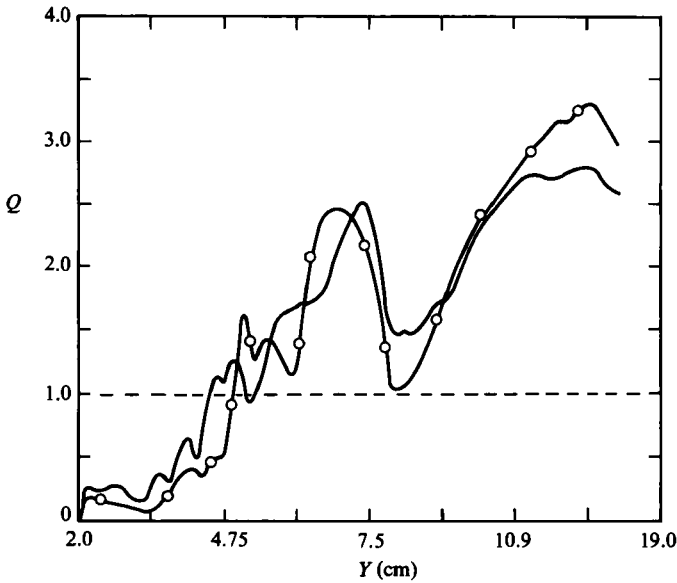


FIGURE 12. Ratio of fluorescent areas as a function of the streamwise direction at 0.96 ms, for  $V_s/V_f = 0.1$  and  $V_f = 2.0 \times 10^4$  cm/s; solid line:  $6.13 \times 19.44$  cm<sup>2</sup> domain, solid line with circles:  $22.3 \times 24.9$  cm<sup>2</sup> domain.

line is for an outflow-boundary condition in which the pressure at the outflow boundary relaxes to its background value, as given in (1). The solid line with circles is for calculations in which the streamwise pressure gradient was set equal to zero at the outflow. In this case (zeroth-order extrapolation) we neglected the second term on the right-hand side of (1). Although this condition is unphysical, it gives a useful limiting case. For the times considered, the differences between the curves are only slight, showing that the results are insensitive to changes in the outflow-boundary

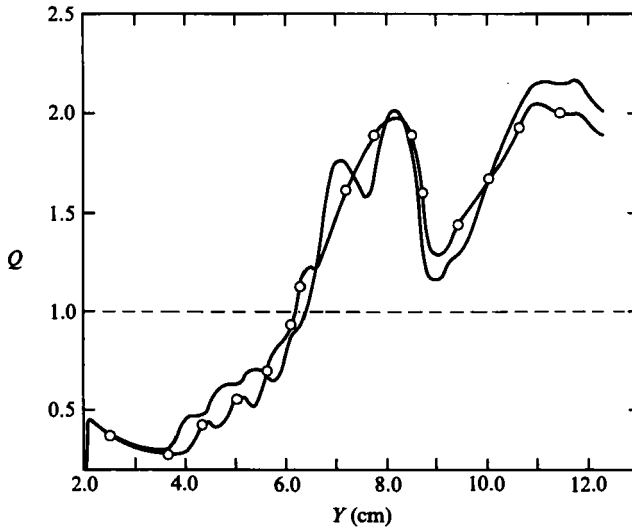


FIGURE 13. Ratio of fluorescent areas as a function of the streamwise direction at 1.73 ms, for  $V_s/V_f = 0.2$  and  $V_f = 1.0 \times 10^4$  cm/s; solid line: relaxation of outflow boundary pressure using (1); solid line with circles: zeroth-order extrapolation of the outflow boundary pressure.

conditions. The pattern of asymmetry is essentially the same. The figure shows, however, that the effect of the zeroth-order-pressure-extrapolation condition at this stage is to tend to smooth the structures.

## 5. Discussion and summary

This paper has presented numerical simulations of the evolution of the Kelvin–Helmholtz instability for a splitter-plate geometry. These calculations were performed using the Eulerian, explicit Flux-Corrected Transport algorithm to solve the convective-transport problem. New boundary conditions were developed to allow the inflowing material to respond to pressure fluctuations occurring in the computational region. New boundary conditions were also developed for the outflow to model the relaxation of the gas in the computational domain to the unperturbed ambient gas.

The focus of this paper is the evolution of the coherent structures in spatially evolving mixing layers, with particular emphasis on their composition. The computations show a trend in which more fast fluid than slow fluid is entrained in the structures. This asymmetry is larger as the velocity ratio of the two streams increases. The calculated effect is consistent with the experimental results of Koochesfahani *et al.* (1983), discussed above. We note, however, that the experiments were done using liquids, while the calculations considered a fast-moving (but subsonic) gas. In addition, the computational model only measures the large-scale features of the mixing layers, i.e. convective mixing, since molecular diffusion is not included.

The asymmetric entrainment is a feature inherently associated to spatially evolving mixing layers and due to the symmetry-breaking development of the downstream coherent vortical structures, which draw in more faster than slower fluid. Hence, it cannot occur in simulations with periodic boundary conditions involving equal and opposite velocities. The asymmetry depends directly on the free-stream velocity ratio, and should tend to disappear as the ratio tends to unity. This general trend is shown by our results, in spite of the rather small velocity ratios considered.

The co-flowing system of two streams of air described above is unstable as long as the Reynolds number is high enough and there is some small perturbation in the system. This perturbation can be an imposed frequency at the beginning of the calculation, or simply noise or round-off error. Because feedback is allowed between the downstream events and the inflow boundary conditions through the zero-pressure-gradient condition at the inflow, there is no need to constantly drive the instability.

The mechanism which reinitiates the instabilities close to the inflow boundary works through pressure pulses generated at various scales by the fluid accelerations caused by downstream vortex roll-ups and mergings. They are required to ensure that the flow remains essentially divergence-free everywhere when a coherent structure or vortex is locally accelerated. Though these pulses are transmitted acoustically, they exist even in the incompressible limit.

Evidence supporting this mechanism is given by the sequences of panels shown in figures 4 and 5. The flow structure at 0.975 ms, for example, is both large and irregular enough to generate pressure perturbations, which drive noticeable fluctuations throughout the computational region. In addition, the reflection of the pressure pulses on the confining walls affects the development of the larger structures which, in turn, influence the pattern of formation of new structures upstream. A feedback mechanism, in which the upstream flow is influenced by the downstream, was proposed by Dimotakis & Brown (1976). This was used to explain unusually long autocorrelation times of the streamwise velocity fluctuations observed in the experiments. These could not be explained by a local flow property.

A number of tests were made to evaluate the importance of the resolution and size of the computational region and the location of the solid bounding walls to the mixing asymmetry. The resolution tests showed that the large-scale features and the mixing asymmetry reported above were adequately resolved by the computational grid chosen. The locations of the bounding walls did not appear to affect the basic calculated mixing asymmetry. Also, the mixing asymmetry results were not particularly sensitive to the choice of the outflow-boundary conditions, although using a physically correct inflow-boundary condition is extremely important.

The accuracy of the FCT calculations on variably spaced grids has been tested extensively. This was discussed in §3.1. It is important, however, to consider what the variable grid might do for the splitter-plate calculations presented here. We know that, as the structures in the calculations move into more widely spaced zones, short-wavelength information is damped. Also, as the spectrum of pressure disturbances created by roll-ups and mergings moves into more finely resolved regions from coarser regions, it is missing a portion of its short-wavelength spectrum that it would have if the zones downstream were finer. The result we have seen is that the large-scale structures and features of the asymmetry are not significantly affected by the grid spacings. Future investigations will look at the finer details of how the re-initiation process might be affected by these missing short wavelengths propagating from downstream.

The exact structure of the unstable flow at a given time is very sensitive to background conditions, initial conditions, and to small fluctuations in the system. This is the crux of the problem in experiments also: many realizations are possible depending on fluctuations in the initial and boundary conditions. Thus, we observe that some of the difficulty encountered in the computations reflects the same difficulty in the experiments. Both highlight the highly nonlinear sensitivity of the system to the boundary and initial conditions.

We would like to thank Drs K. Kailasanath, R. H. Guirguis and M. J. Fritts for many stimulating and illuminating discussions, and to C. E. Oswald, R. J. Scott, and Drs J. M. Picone and T. R. Young for their invaluable help implementing the FAST2D code and the various diagnostics used in this work. We would also like to thank Professors N. Chigier and A. Roshko for encouraging this project. The calculations were performed under Office of Naval Research project RR024-03-01 and Naval Research Laboratory project RR011-09-43.

## REFERENCES

- ASHURST, W. T. 1979 Numerical simulation of turbulent mixing layers via vortex dynamics. In *Turbulent Shear Flows* (ed. F. Durst, B. E. Launder, F. W. Schmit & J. H. Whitelaw), vol. 1, pp. 402–413. Springer-Verlag.
- BOOK, D. L., BORIS, J. P., KUHL, A., ORAN, E. S., PICONE, J. M. & ZALESK, S. 1980 Simulation of complex shock reflections from wedge in inert and reactive gas mixtures. In *Proceedings of the 7th International Conference on Numerical Methods in Fluid Dynamics*, pp. 84–90. Springer-Verlag.
- BORIS, J. P. 1976*a* Flux corrected transport modules for solving generalized continuity equations. *Naval Res. Lab. Mem. Rep.* 3237.
- BORIS, J. P. 1976*b* Numerical solution of continuity equations. *Comp. Phys. Commun.* **12**, 67.
- BORIS, J. P. & BOOK, D. L. 1976 Solution of continuity equations by the method of flux corrected transport. In *Methods in Computational Physics*, vol. 16, pp. 85–129. Academic.
- BORIS, J. P., ORAN, E. S., GARDNER, J. H., GRINSTEIN, F. F. & OSWALD, C. E. 1985 Direct simulations of spatially evolving compressible turbulence – techniques and results. In *Ninth International Conference on Numerical Methods in Fluid Dynamics* (ed. Soubbaramayer & J. P. Boujot), pp. 98–102. Springer-Verlag.
- BREIDENTHAL, R. 1981 Structure in turbulent mixing layers and wakes using a chemical reaction. *J. Fluid Mech.* **109**, 1.
- BROADWELL, J. E. & BREIDENTHAL, R. E. 1982 A simple model of mixing and chemical reaction in a turbulent shear layer. *J. Fluid Mech.* **125**, 397.
- BROWAND, F. K. & WEIDMAN, P. D. 1976 Large scales in the developing mixing-layer. *J. Fluid Mech.* **76**, 127.
- BROWAND, F. K. & WINANT, C. D. 1973 Laboratory observations of shear layer instability in a stratified fluid. *Boundary-Layer Met.* **5**, 67.
- BROWN, G. & ROSHKO, A. 1974 On density effects and large structure in turbulent mixing layers. *J. Fluid Mech.* **64**, 775.
- DAVIS, R. W. & MOORE, E. F. 1985 A numerical study of vortex merging in mixing layers. *Phys. Fluids* **28**, 1626.
- DIMOTAKIS, P. E. & BROWN, G. L. 1976 The mixing layer at high Reynolds number: large structure dynamics and entrainment. *J. Fluid Mech.* **78**, 535.
- FREYMUTH, P. 1966 On transition in a separated laminar boundary layer. *J. Fluid Mech.* **25**, 683.
- FYFE, D. E., GARDNER, J. H., PICONE, M. & FRY, M. A. 1985 Fast three-dimensional Flux-Corrected Transport code for highly resolved compressible flow calculations. In *Ninth International Conference on Numerical Methods in Fluid Dynamics* (ed. Soubbaramayer & J. P. Boujot), pp. 230–234. Springer-Verlag.
- HO, C. M. & HUANG, L. S. 1982 Subharmonics and vortex merging in mixing layers. *J. Fluid Mech.* **119**, 443.
- HO, C. M. & HUERRE, P. 1984 Perturbed free shear layers. *Ann. Rev. Fluid Mech.* **16**, 365.
- KAILASANATH, K. & ORAN, E. 1985*a* A computational method for determining cell size. *AIAA paper* 85-0236.
- KAILASANATH, K. & ORAN, E. 1985*b* Determination of detonation cell size and the role of transverse waves in two-dimensional detonations. To appear in *Comb. Flame*.

- KONRAD, J. H. 1976 An experimental investigation of mixing in two dimensional turbulent shear flows with applications to diffusion-limited chemical reactions. *Project SQUID Tech. Rep. CIT-8-PU*.
- KOOCHESFAHANI, M. M., DIMOTAKIS, P. E. & BROADWELL, J. E. 1983 Chemically reacting turbulent shear layers. *AIAA paper 83-0475*. New York.
- LANDAU, L. D. & LIFTSHITZ, E. M. 1959 *Fluid Mechanics*. Pergamon.
- LIEPMANN, N. W. 1979 The rise and fall of ideas in turbulence. *Am. Scient.* **67**, 221.
- ORAN, E. S. & BORIS, J. P. 1981 Detailed modelling of combustion system. *Prog. Energy Combustion Sci.* **7**, 1.
- ORAN, E. S., YOUNG, T. R., BORIS, J. P., PICONE, J. M. & EDWARDS, D. H. 1982 *Nineteenth Symposium (International) on Combustion*, p. 573. The Combustion Institute, Pittsburgh.
- PICONE, J. M. & BORIS, J. P. 1983 Vorticity generation by asymmetric energy deposition in a gaseous medium. *Phys. Fluids* **26**, 365.
- RAYLEIGH, LORD 1880 *Proc. Lond. Math. Soc.* **11**, 57-70. Reprinted (1899) in *Sci. Papers*, vol. 1, p. 474. Cambridge University Press.
- RILEY, J. J. & METCALFE, R. W. 1980 Direct numerical simulation of a perturbed, turbulent mixing layer. *AIAA paper 80-0274*. Pasadena.
- ROSHKO, A. 1976 Structure of turbulent shear flows: a new look. *AIAA J.* **14**, 1349.
- TURKEL, E. 1980 Numerical methods for large-scale time-dependent partial differential equations. In *Computational Fluid Dynamics* (ed. W. Kollman), pp. 128-262. Hemisphere Press, Washington DC.
- WINANT, C. D. & BROWAND, F. K. 1974 Vortex pairing: the mechanism of turbulent mixing layer growth at moderate Reynolds number. *J. Fluid Mech.* **63**, 237.
- WYGNANSKI, I. & FIEDLER, H. 1970 The two-dimensional mixing region. *J. Fluid Mech.* **41**, 327.
- ZABUSKY, N. J. 1981 Computational synergetics and mathematical innovation. *J. Comp. Phys.* **43**, 195.